Electronic properties of graphene/hexagonal-boron-nitride moiré superlattice

Pilkyung Moon[*]

New York University Shanghai, Pudong, Shanghai 200120, China

Mikito Koshino

Department of Physics, Tohoku University, Sendai, 980-8578, Japan

We theoretically investigate the electronic structures of moiré superlattices arising in monolayer/bilayer graphene stacked on hexagonal boron nitride (hBN) in the presence and absence of magnetic field. We develop an effective continuum model from a microscopic tight-binding lattice Hamiltonian and calculate the electronic structures of graphene-hBN systems with different rotation angles. Using the effective model, we explain the characteristic band properties such as the gap opening at the corners of the superlattice Brillouin zone (mini-Dirac point). We also investigate the energy spectrum and quantum Hall effect of graphene-hBN systems in uniform magnetic field and demonstrate the evolution of the fractal spectrum as a function of the magnetic field. The spectrum generally splits in the valley degrees of freedom (K and K') due to the lack of the inversion symmetry, and the valley splitting is more significant in bilayer graphene on hBN than in monolayer graphene on hBN because of the stronger inversion-symmetry breaking in bilayer.

I. INTRODUCTION

Whenever two atomically-thin lattices are stacked in an incommensurate manner, there always arises a superlattice structure which modulates along the in-plane direction due to the moiré interference between different lattice periods. For example, a bilayer graphene stacked at an arbitrary angle (twisted bilayer graphene) [1] exhibits a periodic variation of the interlayer interaction in the form of moiré pattern, of which the period can exceed the range of the atomic scale. The electronic structures of twisted bilayer graphenes have been intensively investigated, and it is shown that the material properties, such as the Fermi velocity, the band energy scale, and optical absorption spectrum, can be widely tunable with respect to the twist angle [2–10]. Moreover, a huge unit cell of moiré superlattice provides an opportunity to investigate the self-similar, fractal evolution of the energy spectrum [11] under the simultaneous influences of spatial period and magnetic field [12–14].

Recently, the graphene stacked on hexagonal boron nitride (hBN) has attracted much attention as another moiré superlattice system [15–21]. Hexagonal boron nitride is isostructural to graphene but has boron and nitrogen atoms at A and B sublattices, respectively, leading to a finite energy gap in the electronic structure [22,23]. When the graphene is placed on the hBN substrate, the 1.8% lattice mismatch between graphene and hBN introduces a superlattice potential even in a nonrotated stacking. The transport properties in graphene-hBN systems have been investigated experimentally, and in particular, the fractal electronic structure was actually observed in magnetic fields [18–20,24]. The electronic structures of graphene-hBN systems have been studied using several theoretical approaches [25–37]. The effective model was derived from the extension from the twisted bilayer graphene [26], the symmetry based approach [28,29], and also

from the density functional theory [32]. The energy spectrum in the magnetic field in the presence of hBN-substrate was also calculated [18–20,24].

In this paper, we theoretically investigate the electronic structures of moiré superlattices arising in monolayer and bilayer graphene stacked on the hBN layer with and without magnetic field. We develop an effective continuum model starting from a microscopic tight-binding lattice Hamiltonian and calculate the electronic structures of graphene-hBN systems with several different rotation angles. The model is expressed in terms of a few parameters, which are analytically extracted from the microscopic parameters in the given tight-binding model. We verify the validity of the effective model by demonstrating that the calculated band structure agrees with that of the original tight-binding model. In the band structure calculation, we find that we generally have a band gap at the zone corners of the superlattice Brillouin zone (so-called mini-Dirac point) due to the inversion symmetry breaking, and the gap width is shown to be greater in the hole side than in the electron side. We analytically explain the origin of the electron-hole asymmetric gap opening in terms of the matrix elements of the effective model.

We then study the energy spectrum and quantum Hall effect of graphene-hBN systems in uniform magnetic fields and demonstrate the evolution of the fractal spectrum as a function of the magnetic field. We find that the spectrum generally splits in the valley degrees of freedom (K and K') due to the lack of the inversion symmetry. The valley splitting is more significant in bilayer graphene on hBN than in monolayer graphene on hBN, because the inversion symmetry is severely broken in the bilayer case, where only a single layer out of two graphene layers feels the effective potential from hBN.

The paper is organized as follow. In Sec. II, we derive an effective continuum model for graphene on hBN structures from a tight-binding Hamiltonian. On the basis of the effective and tight-binding models, we study the band structures of both monolayer and bilayer graphene on hBN in Sec. III. In Sec. IV, we investigate the fractal energy spectrum and the

---

[*]pilkyung.moon@nyu.edu

quantum Hall effect of electrons under magnetic field. Finally, conclusions are given in Sec. V.

II. THEORETICAL METHODS

A. Atomic structure and moiré lattice vectors

We consider a bilayer system composed of graphene and hBN. Graphene is a two-dimensional honeycomb lattice of carbon atoms, of which the unit cell includes A and B sublattices. The hBN is a similar honeycomb lattice but composed of nitride atom on A site and boron atom on B site. The lattice constant (i.e., the distance between the nearest A sites) of hBN is given by $a_{\mathrm{hBN}} \approx 0.2504$ nm [38], which is slightly larger than $a \approx 0.246$ nm for graphene. We assume that the interlayer distance between graphene and hBN is constant at $d_{\mathrm{G\text{-}hBN}} = 0.322$ nm [39].

We define the stacking geometry of the graphene-hBN bilayer system by starting from a nonrotated arrangement, where a B site of graphene and a B site of hBN share the same in-plane position $(x, y) = 0$, and the A-B bonds are parallel to each other. We then rotate the hBN with respect to graphene by an arbitrary angle θ around the origin. We define $\mathbf{a}_1 = a(1, 0)$ and $\mathbf{a}_2 = a(1/2, \sqrt{3}/2)$ as the lattice vectors of graphene. The primitive lattice vectors of hBN become

$$\tilde{\mathbf{a}}_i = M R \, \mathbf{a}_i \quad (i = 1, 2), \tag{1}$$

where R is the rotation matrix by θ, and $M = (1 + \varepsilon)\mathbf{1}$ represents the isotropic expansion by the factor $1 + \varepsilon = a_{\mathrm{hBN}}/a \approx 1.018$. We define the reciprocal lattice vectors $\mathbf{a}_i^*$ and $\tilde{\mathbf{a}}_i^*$ for graphene and hBN, respectively, so as to satisfy $\mathbf{a}_i \cdot \mathbf{a}_j^* = \tilde{\mathbf{a}}_i \cdot \tilde{\mathbf{a}}_j^* = 2\pi \delta_{ij}$.

The mismatch of the lattice periods of graphene and hBN gives rise to the moiré interference pattern. An atom on hBN located at position $\mathbf{r}$ has its counterpart on graphene at $R^{-1}M^{-1} \mathbf{r}$. The displacement vector between two sites (from graphene to hBN) is

$$\boldsymbol{\delta}(\mathbf{r}) = (\mathbf{1} - R^{-1}M^{-1})\mathbf{r}. \tag{2}$$

When $\boldsymbol{\delta}(\mathbf{r})$ coincides with a lattice vector of graphene, then graphene and hBN share the same phase of the lattice periodicity (i.e., the corresponding positions of their hexagonal unit cells) at the position $\mathbf{r}$, in the same way as in the origin. Therefore, the primitive lattice vector of the moiré superlattice $\mathbf{L}_i^{\mathrm{M}}$ is obtained from the condition $\boldsymbol{\delta}(\mathbf{L}_i^{\mathrm{M}}) = \mathbf{a}_i$, which leads to

$$\mathbf{L}_i^{\mathrm{M}} = (\mathbf{1} - R^{-1}M^{-1})^{-1}\mathbf{a}_i \quad (i = 1, 2). \tag{3}$$

The corresponding moiré reciprocal lattice vectors satisfying $\mathbf{G}_i^{\mathrm{M}} \cdot \mathbf{L}_j^{\mathrm{M}} = 2\pi \delta_{ij}$ are written as

$$\mathbf{G}_i^{\mathrm{M}} = (\mathbf{1} - M^{-1}R)\mathbf{a}_i^* \quad (i = 1, 2), \tag{4}$$

where we used $R^\dagger = R^{-1}$ and $M^\dagger = M$. The moiré lattice period $L^{\mathrm{M}} = |\mathbf{L}_1^{\mathrm{M}}| = |\mathbf{L}_2^{\mathrm{M}}|$ is [17]

$$L^{\mathrm{M}} = \frac{1 + \varepsilon}{\sqrt{\varepsilon^2 + 2(1 + \varepsilon)(1 - \cos\theta)}} \, a, \tag{5}$$

and the angle from $\mathbf{a}_i$ to $\mathbf{L}_i^{\mathrm{M}}$ is

$$\phi = \arctan\left(\frac{-\sin\theta}{1 + \varepsilon - \cos\theta}\right). \tag{6}$$

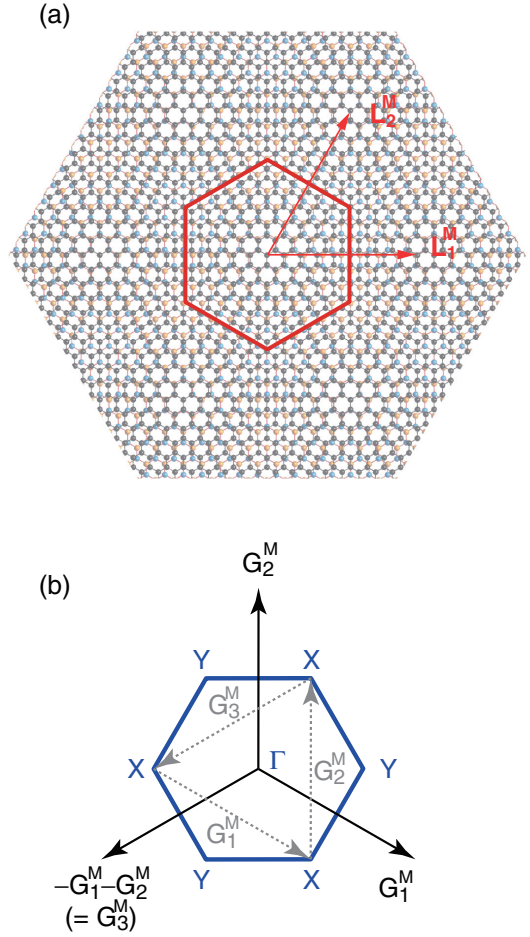
FIG. 1. (Color online) (a) Graphene-hBN moiré superlattice with $\theta = 0°$ and an exaggerated lattice constant ratio $a_{\mathrm{hBN}}/a = 10/9$. Unit cell is indicated by a hexagon. (b) Superlattice Brillouin zone with the reciprocal lattice vectors spanned by $\mathbf{G}_i^{\mathrm{M}}$.

When $\theta = 0°$, we have $L^{\mathrm{M}} = 13.8$ nm. Figure 1(a) shows the atomic structure and unit cell of graphene-hBN moiré with $\theta = 0°$ and an exaggerated lattice constant ratio $a_{\mathrm{hBN}}/a = 10/9$. Figure 1(b) is the superlattice Brillouin zone spanned by $\mathbf{G}_i^{\mathrm{M}}$.

B. Tight-binding model

We consider the tight-binding model for p_z atomic orbitals. The Hamiltonian is written as

$$H = -\sum_{i,j} t(\mathbf{R}_i - \mathbf{R}_j)|\mathbf{R}_i\rangle\langle\mathbf{R}_j| + \sum_i V(\mathbf{R}_i)|\mathbf{R}_i\rangle\langle\mathbf{R}_i|, \tag{7}$$

where $\mathbf{R}_i$ and $|\mathbf{R}_i\rangle$ represent the lattice point and the atomic state at site i, respectively, $V(\mathbf{R}_i)$ is the on-site potential at site i, and $t(\mathbf{R}_i - \mathbf{R}_j)$ is the transfer integral between the sites i and j. We assume $V_{\mathrm{C}} = 0$ for carbon atom, and

$$V_{\mathrm{B}} = 3.34 \text{ eV}, \quad V_{\mathrm{N}} = -1.40 \text{ eV}, \tag{8}$$

for boron and nitride atoms, respectively [40].

For the transfer integral, we simply adopt the common Slater-Koster-type function for any combinations of atomic

species [3,41–43],

$$-t(\mathbf{R}) = V_{pp\pi}\left[1 - \left(\frac{\mathbf{R}\cdot\mathbf{e}_z}{R}\right)^2\right] + V_{pp\sigma}\left(\frac{\mathbf{R}\cdot\mathbf{e}_z}{R}\right)^2,$$

$$V_{pp\pi} = V_{pp\pi}^0 \exp\left(-\frac{R - a_0}{r_0}\right), \tag{9}$$

$$V_{pp\sigma} = V_{pp\sigma}^0 \exp\left(-\frac{R - d_0}{r_0}\right).$$

Here $\mathbf{e}_z$ is the unit vector perpendicular to the graphene plane, $a_0 = a/\sqrt{3} \approx 0.142$ nm is the distance of neighboring A and B sites on graphene, and $d_0 \approx 0.335$ nm is the interlayer spacing of graphene. $V_{pp\pi}^0$ is the transfer integral between the nearest-neighbor atoms of monolayer graphene and $V_{pp\sigma}^0$ is that between vertically located atoms on the neighboring layers. We take $V_{pp\pi}^0 \approx -2.7$ eV, $V_{pp\sigma}^0 \approx 0.48$ eV to fit the dispersions of monolayer graphene and AB-stacked bilayer graphene [3]. r_0 is the decay length of the transfer integral, and is chosen as $0.184a$ so that the next nearest intralayer coupling becomes $0.1V_{pp\pi}^0$ [3,42].

In the tight-binding band calculation, the lattice structure of a graphene-hBN composite system must have a finite unit cell, and for this purpose we take $\theta = 0$ and rationalize the relative lattice period $a_{\text{hBN}}/a \approx 1.018$ to 56/55. We do not need the lattice rationalization in the continuum model argued in the next section, where the atomic period a is smeared out and the Hamiltonian is governed only by L^{M}.

Figure 2(a) illustrates the Brillouin zone (BZ) folding where a_{hBN}/a is taken as 5/4 (instead of 56/55) for the illustrative
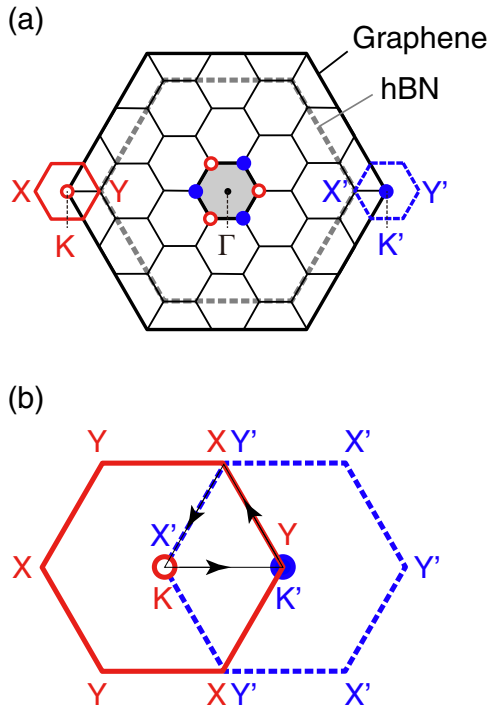

FIG. 2. (Color online) (a) Brillouin zone (BZ) folding in graphene-hBN moiré superlattice, where a_{hBN}/a is taken as 5/4 for the illustrative purpose. (b) Relative positions of the BZs centered at K and K' valleys in the common BZ.

purpose. The solid large hexagon is the graphene's BZ spanned by $\mathbf{a}_i^*$, and the small hexagon is the reduced BZ spanned by $\mathbf{G}_i^{\text{M}}$. In the tight-binding model, K and K' are inseparable and all the energy bands are folded in the common BZ. In the continuum model, on the other hand, K and K' valleys are treated independently, and the energy bands can be separately plotted in the BZ centered at K (red, solid) and that centered at K' (blue, dashed). Figure 2(b) shows the relation between the separate BZs in the original common BZ.[1]

C. Effective continuum model

When the rotation angle θ is small and the moiré superlattice period L^{M} is much larger than the lattice constant a, the interaction between the two graphene layers is dominated by long-wavelength components, allowing one to treat the problem in the effective continuum model. In the literature, the continuum approach has been introduced for the twisted graphene-graphene bilayer [2,6,7,9,10] and also for the graphene-hBN system [26,28,32]. Here we derive an effective continuum model starting from the microscopic tight-binding Hamiltonian using the approach developed for the twisted graphene bilayer [10]. The effective Hamiltonian is expressed in terms of a few parameters, which are directly extracted from the microscopic parameters in the given tight-binding model.

The low-energy spectrum of graphene is dominated by the states near K and K' points, and the effective Hamiltonian is approximated by the effective Dirac cones centered at those points [44–48]. In the present case, the K points of graphene are located at $\mathbf{K}_\xi = -\xi(2\mathbf{a}_1^* + \mathbf{a}_2^*)/3$ where $\xi = \pm 1$ for K and K', respectively. The Hamiltonian of monolayer graphene near $\mathbf{K}_\xi$ is written as

$$H_{\text{G}} \approx -\hbar v \mathbf{k} \cdot \boldsymbol{\sigma}_\xi, \tag{10}$$

where $\mathbf{k}$ is the relative wave number measured from $\mathbf{K}_\xi$ point, and $\boldsymbol{\sigma}_\xi = (\xi\sigma_x, \sigma_y)$ with Pauli matrices σ_x and σ_y. The parameter v is the band velocity of the Dirac cone, which is given in the present tight-binding parametrization as $v \approx (\sqrt{3}a/2\hbar)V_{pp\pi}^0(1 - 2e^{-a_0/r_0}) \approx 0.80 \times 10^6$ m/s [10].

K valleys of hBN are given by $\tilde{\mathbf{K}}_\xi = -\xi(2\tilde{\mathbf{a}}_1^* + \tilde{\mathbf{a}}_2^*)/3$. The effective Hamiltonian of hBN monolayer includes a similar kinetic term linear to the relative wave number from $\tilde{\mathbf{K}}_\xi$, plus the on-site potential term V_{N} and V_{B}. This gives a massive Dirac cone separated by an energy gap $V_{\text{B}} - V_{\text{N}}$ with a quadratic dispersion centered at $\tilde{\mathbf{K}}_\xi$. Here we adopt an approximation in which we completely neglect the dispersion of hBN by dropping $\mathbf{k}$ [26], i.e.,

$$H_{\text{hBN}} \approx \begin{pmatrix} V_{\text{N}} & 0 \\ 0 & V_{\text{B}} \end{pmatrix}. \tag{11}$$

This is justified when θ is small, because $\mathbf{K}_\xi$ and $\tilde{\mathbf{K}}_\xi$ are then close to each other, and the graphene's electronic states near $\mathbf{K}_\xi$ are coupled only with the hBN's states near $\tilde{\mathbf{K}}_\xi$ by the long-range interlayer coupling.

---

[1]The relative position of K and K' in the folded BZ actually depends on the rounded value of L^{M}/a in the modulo 3, and it is equivalent in the exaggerated $a_{\text{hBN}}/a = 5/4$ and in the original 56/55.

The interlayer coupling term between graphene and hBN can be derived in a similar manner to the twisted bilayer graphene [10]. When θ is small, the local lattice structure is approximately viewed as a pair of identical honeycomb lattices shifted by a displacement vector $\boldsymbol{\delta}$ with no rotation. $\boldsymbol{\delta}$ slowly depends on the position $\mathbf{r}$ in accordance with Eq. (2). The interlayer coupling term for the nonrotated honeycomb bilayer with a constant $\boldsymbol{\delta}$ can be derived from a tight-binding model in a straightforward manner, which is described in the Appendix A. By replacing constant $\boldsymbol{\delta}$ with $\boldsymbol{\delta}(\mathbf{r})$, we obtain the interlayer Hamiltonian for the moiré system. As a result, the effective Hamiltonian of the graphene-hBN system near the $\mathbf{K}_\xi$ point is written as

$$\mathcal{H}_{\text{G-hBN}} = \begin{pmatrix} H_{\text{G}} & U^\dagger \\ U & H_{\text{hBN}} \end{pmatrix}, \tag{12}$$

with

$$U = \begin{pmatrix} U_{A_2 A_1} & U_{A_2 B_1} \\ U_{B_2 A_1} & U_{B_2 B_1} \end{pmatrix} = u_0 \left[\begin{pmatrix} 1 & 1 \\ 1 & 1 \end{pmatrix} \right. \\ \left. + \begin{pmatrix} 1 & \omega^{-\xi} \\ \omega^\xi & 1 \end{pmatrix} e^{i\xi \mathbf{G}_1^{\text{M}} \cdot \mathbf{r}} + \begin{pmatrix} 1 & \omega^\xi \\ \omega^{-\xi} & 1 \end{pmatrix} e^{i\xi (\mathbf{G}_1^{\text{M}} + \mathbf{G}_2^{\text{M}}) \cdot \mathbf{r}} \right], \tag{13}$$

and $\omega = \exp(2\pi i/3)$. Here the 4×4 matrix is written for the basis of $\{A_1, B_1, A_2, B_2\}$, with A_1, B_1 for graphene, A_2, B_2 for hBN. The only parameter u_0 is defined by the in-plane Fourier transform of the transfer integral $t(\mathbf{R})$,

$$u_0 = \frac{1}{S} \int t(\mathbf{R} + \mathbf{d}_z) e^{-i\mathbf{K}_\xi \cdot \mathbf{R}} d\mathbf{R}, \tag{14}$$

where $S = |\mathbf{a}_1 \times \mathbf{a}_2|$ is the unit cell area, $\mathbf{d}_z = d_{\text{G-hBN}} \mathbf{e}_z$ is the perpendicular displacement between graphene and hBN, and the integral in $\mathbf{R}$ is taken over an infinite two-dimensional space. The u_0 does not depend on ξ, and we have $u_0 \approx 0.152$ eV in the present tight-binding parameters.

Since the energy band of hBN is gapped, the low-energy spectrum near $E \approx 0$ is dominated by graphene's electronic states. Then the effective Hamiltonian is even reduced to a 2×2 form by eliminating the hBN bases by the second order perturbation. The result is

$$\mathcal{H}_{\text{G-hBN}}^{(\text{red})} = H_{\text{G}} + U^\dagger (-H_{\text{hBN}})^{-1} U \\ \equiv H_{\text{G}} + V_{\text{hBN}}, \tag{15}$$

where the additional term V_{hBN} is explicitly written as

$$V_{\text{hBN}} = V_0 \begin{pmatrix} 1 & 0 \\ 0 & 1 \end{pmatrix} \\ + \left\{ V_1 e^{i\xi\psi} \left[\begin{pmatrix} 1 & \omega^{-\xi} \\ 1 & \omega^{-\xi} \end{pmatrix} e^{i\xi \mathbf{G}_1^{\text{M}} \cdot \mathbf{r}} + \begin{pmatrix} 1 & \omega^\xi \\ \omega^\xi & \omega^{-\xi} \end{pmatrix} e^{i\xi \mathbf{G}_2^{\text{M}} \cdot \mathbf{r}} \right. \right. \\ \left. \left. + \begin{pmatrix} 1 & 1 \\ \omega^{-\xi} & \omega^{-\xi} \end{pmatrix} e^{-i\xi (\mathbf{G}_1^{\text{M}} + \mathbf{G}_2^{\text{M}}) \cdot \mathbf{r}} \right] + \text{H.c.} \right\}, \tag{16}$$

and

$$V_0 = -3u_0^2 \left(\frac{1}{V_{\text{N}}} + \frac{1}{V_{\text{B}}} \right), \tag{17}$$

$$V_1 e^{i\psi} = -u_0^2 \left(\frac{1}{V_{\text{N}}} + \omega \frac{1}{V_{\text{B}}} \right). \tag{18}$$

In the present parameters, we have $V_0 \approx 0.0289$ eV, $V_1 \approx 0.0210$ eV, and $\psi \approx -0.29$(rad).

The effective term V_{hBN} can be generally divided into the scalar potential V^{eff}, the vector potential $\mathbf{A}^{\text{eff}}$, and the Dirac mass term M^{eff} as [26,28]

$$V_{\text{hBN}} = V^{\text{eff}}(\mathbf{r}) + M^{\text{eff}}(\mathbf{r})\sigma_z + ev\mathbf{A}^{\text{eff}}(\mathbf{r}) \cdot \boldsymbol{\sigma}_\xi. \tag{19}$$

For the present V_{hBN} of Eq. (16), we have

$$V^{\text{eff}}(\mathbf{r}) = V_0 - V_1 \sum_{l=1}^3 \cos \alpha_l(\mathbf{r})$$

$$M^{\text{eff}}(\mathbf{r}) = \sqrt{3} V_1 \sum_{l=1}^3 \sin \alpha_l(\mathbf{r}) \tag{20}$$

$$ev\mathbf{A}^{\text{eff}}(\mathbf{r}) = 2\xi V_1 \sum_{l=1}^3 \begin{pmatrix} \cos[2\pi(l+1)/3] \\ \sin[2\pi(l+1)/3] \end{pmatrix} \cos \alpha_l(\mathbf{r})$$

with

$$\alpha_l(\mathbf{r}) = \mathbf{G}_l^{\text{M}} \cdot \mathbf{r} + \psi + \frac{2\pi}{3}, \tag{21}$$

where we defined $\mathbf{G}_3^{\text{M}} = -\mathbf{G}_1^{\text{M}} - \mathbf{G}_2^{\text{M}}$ so that the vectors $\mathbf{G}_1^{\text{M}}$, $\mathbf{G}_2^{\text{M}}$, and $\mathbf{G}_3^{\text{M}}$ are pointing to the trigonal symmetric directions. The effective vector potential $\mathbf{A}^{\text{eff}}$ gives the effective magnetic field,

$$B^{\text{eff}}(\mathbf{r}) = \nabla \times \mathbf{A}^{\text{eff}} = \xi B_0 \sum_{l=1}^3 \cos \alpha_l(\mathbf{r}), \tag{22}$$

where

$$B_0 = \frac{2V_1 G^{\text{M}}}{ev} \cos \phi. \tag{23}$$

Here $G^{\text{M}} \equiv |\mathbf{G}_l^{\text{M}}| = (4\pi/\sqrt{3})/L^{\text{M}}$, and ϕ is defined by Eq. (6). The effective magnetic field is opposite between the different valleys $\xi = \pm 1$ due to the time-reversal symmetry. In the present model, the magnitude of the effective magnetic field is $B_0 \sim 0.022$ T at $\theta = 0°$.

The lattice structure of the graphene-hBN hybrid system is not invariant in the spatial inversion, and accordingly, the effective Hamiltonian Eq. (15) lacks the inversion symmetry as shown in the following. The spatial inversion changes $\mathbf{r}$ to $-\mathbf{r}$, and at the same time it swaps A and B sublattices and K and K' valleys. If the system has the inversion symmetry, then the Hamiltonian $H^{(\xi)}(\mathbf{k},\mathbf{r})$ yields to

$$H^{(-\xi)}(\mathbf{k},\mathbf{r}) = \sigma_x [H^{(\xi)}(-\mathbf{k}, -\mathbf{r})]\sigma_x. \tag{24}$$

The Hamiltonian of pristine graphene, Eq. (10), satisfies this condition. For the effective potential terms in Eq. (19), the condition Eq. (24) is rewritten as $V^{\text{eff}}(-\mathbf{r}) = V^{\text{eff}}(\mathbf{r})$, $M^{\text{eff}}(-\mathbf{r}) = -M^{\text{eff}}(\mathbf{r})$, and $\mathbf{A}^{\text{eff}}(-\mathbf{r}) = \mathbf{A}^{\text{eff}}(\mathbf{r})$. The effective
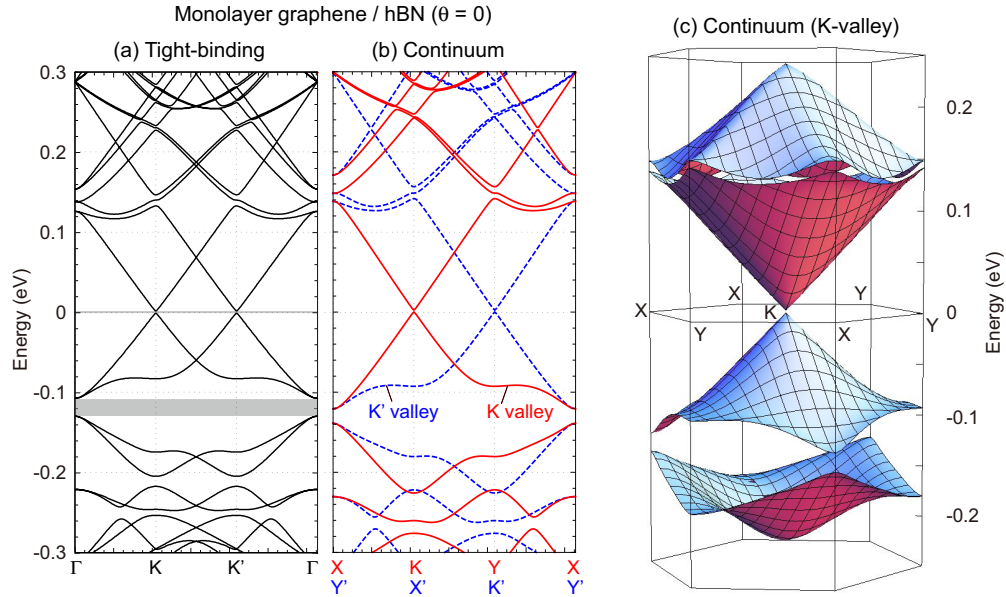
FIG. 3. (Color online) Band structures of monolayer graphene/hBN system with $\theta = 0^\circ$ calculated by (a) the tight-binding model and (b) the effective continuum model, on the k-space path shown in Fig. 2(b). (c) Three-dimensional plot of the first and second electron and hole bands of K-valley, calculated by the continuum model.

terms in Eq. (20) meet these conditions only when $\psi + 2\pi/3 = n\pi$ (n: integer), while it is not the case in the present model ($\psi + 2\pi/3 \approx 0.57\pi$).

We can also consider AB-stacked bilayer graphene + hBN monolayer system using the same approach. Here we number the layer 1, 2 for graphene bilayer where the layer 1 is faced to the hBN layer, and assume that the two graphene layers are stacked so that B_1 site and A_2 site are vertically located as shown in Fig. 10(a). After eliminating the hBN bases in a similar manner, the effective Hamiltonian in the basis of $\{A_1, B_1, A_2, B_2\}$ is written as

$$\mathcal{H}_{\text{BLG-hBN}} = \begin{pmatrix} H_G + V_{\text{hBN}} & U_{\text{BLG}}^\dagger \\ U_{\text{BLG}} & H_G \end{pmatrix}, \quad (25)$$

where U_{BLG} is the interlayer coupling between AB-stacked graphenes [49],

$$U_{\text{BLG}} = \begin{pmatrix} 0 & \gamma_1 \\ -\hbar v_3(\xi k_x - i k_y) & 0 \end{pmatrix}. \quad (26)$$

The parameter γ_1 represents the band splitting and v_3 describes the trigonal warping [49]. In the present tight-binding parameters, we have $\gamma_1 = 0.34$ eV and $v_3 = 0.051 \times 10^6$ m/s.

We have another possibility of graphene AB-stacking in which A_1 site and B_2 site are vertically located, as shown in Fig. 10(b). This is just 180° in-plane rotation of the previous B_1-A_2 stacking, but they are not equivalent when hBN is added to the third layer, since neither graphene bilayer nor hBN are invariant in 180° rotation. The effective Hamiltonian for the second case is obtained by interchanging the off-diagonal blocks in Eq. (25). We find the energy spectra of the two models make no qualitative difference, although they are not identical. In the following calculation, we concentrate on the

case of Eq. (25), while the energy spectrum for the second case is argued in Appendix B.

III. BAND STRUCTURE

First, we calculate the band structure of monolayer graphene-hBN system at $\theta = 0^\circ$, both in the tight-binding model and in the effective continuum model. Figures 3(a) and 3(b) compare the energy band structure calculated by the tight-binding model (with $a_{\text{hBN}}/a = 56/55$) and the effective continuum model, respectively, on the k-space path shown in Fig. 2(b). Here and in the following, the origin of the energy axis is reset to the charge neutral point. We see that the agreement between the two models is almost complete, showing that the effective continuum model describes the detail of the low-energy spectrum quantitatively well. Figure 3(c) is the three-dimensional plot of the first and second electron and hole bands of K-valley, calculated by the continuum model.

In the spectrum, we see a band splitting between the first and the second electron (hole) bands, due to the band anticrossing at the Brillouin zone boundary. The splitting is fairly large in the hole side leading to an actual spectral gap from $E = -0.14$ eV to -0.12 eV, while it is much narrower in the electron side. This feature is consistent with the experiments, showing that the hole side exhibits a stronger resistance peak than the electron side [17,20,24]. At the central Dirac point, there is a tiny energy gap about 2 meV, which is proportional to the third order to the interlayer coupling u_0 [26]. It should be mentioned that the recent experiments [19,50] reported that a much larger band gap opens at the central Dirac point in graphene/hBN systems with small twist angles. There are several theoretical approaches to explain the origin of the band gap in terms of the strain effect [31–33]
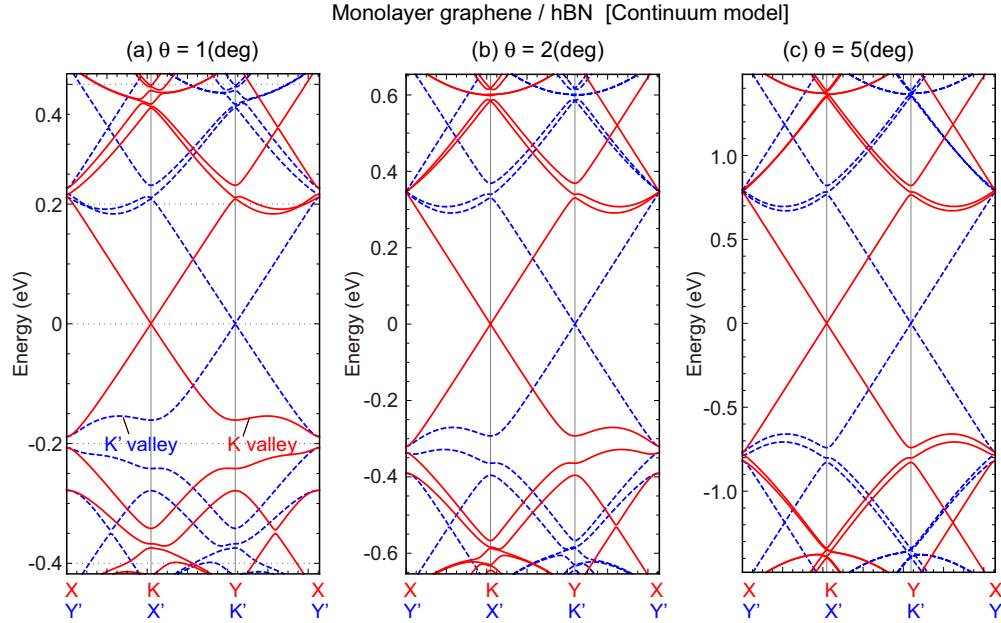
FIG. 4. (Color online) Band structures of a monolayer graphene/hBN system with (a) $\theta = 1°$, (b) $2°$, and (c) $5°$, calculated by the effective continuum model.

and many-body interaction [31] which are not captured in the present calculation.

The gap opening at the Dirac point and the zone corners (mini-Dirac points) is all due to the absence of the inversion symmetry in V_{hBN} which was argued in the previous section. Generally, the coexistence of the spatial inversion symmetry and the time reversal symmetry requires vanishing of the Berry curvature at any nondegenerate points in the energy band, [51,52], and this guarantees the robustness of band touching points in two-dimensional systems [53]. Therefore the original Dirac point at K in intrinsic graphene is never gapped without breaking either the time-reversal or the inversion symmetry. If we have a band touching point under the time-reversal and the inversion symmetries, it requires the existence of another band touching point somewhere in the same energy band. This is because if we only have a single Dirac point in the band, the integrated Berry curvature over the superlattice Brillouin zone except for that Dirac point becomes $\pm\pi$ (from the only Dirac point), and never vanishes.[2] In the present effective Hamiltonian, when V_{hBN} is modified by hand so as to have the inversion symmetry (e.g., ψ is set to $\pi/3$), we actually see that the adjacent bands touch at either of X, Y, or Γ and all the energy bands are connected [28].

The electron-hole asymmetric splitting at the zone corners can be explained by the matrix elements in the effective model. The electronic states at zone corner $X(Y)$ are originally from three k points on the equienergy surface of the intrinsic Dirac cone, and they are mixed by the effective potential V_{hBN}, as shown by dashed arrows in Fig. 1(b). For example, the matrix

element between two X points (denoted as X_1, X_2) connected by $\mathbf{G}_2^M$ in Fig. 1(b) are obtained by

$$\langle X_2 | \; V_1 e^{i\xi\psi} \begin{pmatrix} 1 & \omega^\xi \\ \omega^\xi & \omega^{-\xi} \end{pmatrix} |X_1\rangle, \qquad (27)$$

where $|X_1\rangle$ and $|X_2\rangle$ are Dirac spinors corresponding to the k points, and the matrix in the middle comes from the term having $e^{i\xi\mathbf{G}_2^M \cdot \mathbf{r}}$ in Eq. (16). The matrix elements connecting the triplets are shown to be all identical, and their amplitude determines the energy scale of the band splitting. In $\theta = 0°$, the absolute value of the matrix elements in units of V_1 are shown to be $3/2$ and 2 for X and Y on the hole side, respectively, and they are actually larger than those for the electron side, $1/2$ and 0 for X and Y, respectively.

The continuum model can be easily extended to other twist angles, which are generally hard to treat in the tight-binding model due to the lattice incommensurability. Figure 4 plots the band structures of monolayer graphene + hBN with (a) $\theta = 1°$, (b) $2°$, and (c) $5°$, calculated by the continuum model. We see that the band structures all look similar, while the energy scale expands in increasing θ, according to the increase of the characteristic scale $2\pi\hbar v/L^M$. At the same time, the band splitting, which is of the order of u_0, becomes relatively small compared to the bandwidth.

Figure 5 plots the band structure of AB-stacked bilayer graphene on a hBN system stacked at $\theta = 0°$. We see good agreement between the tight-binding model and the continuum model. Unlike a monolayer graphene-hBN system, we observe a relatively large spectral gap about 40 meV at zero energy, which is accompanied by flat band edges. This is actually due to the interlayer potential difference in bilayer graphene, which is caused by V_0 terms in V_{hBN} for the layer 1. The width of the central gap should also depend on the gate electric field and other electrostatic environments, which contribute to the interlayer potential asymmetry. We also see a band

_____

[2]In the twisted bilayer graphene, in contrast, the lowest energy band has two Dirac points at zero energy (from two K points of the top and bottom layer) so that we can have an energy gap between the first and the second bands even though the system is inversion symmetric.
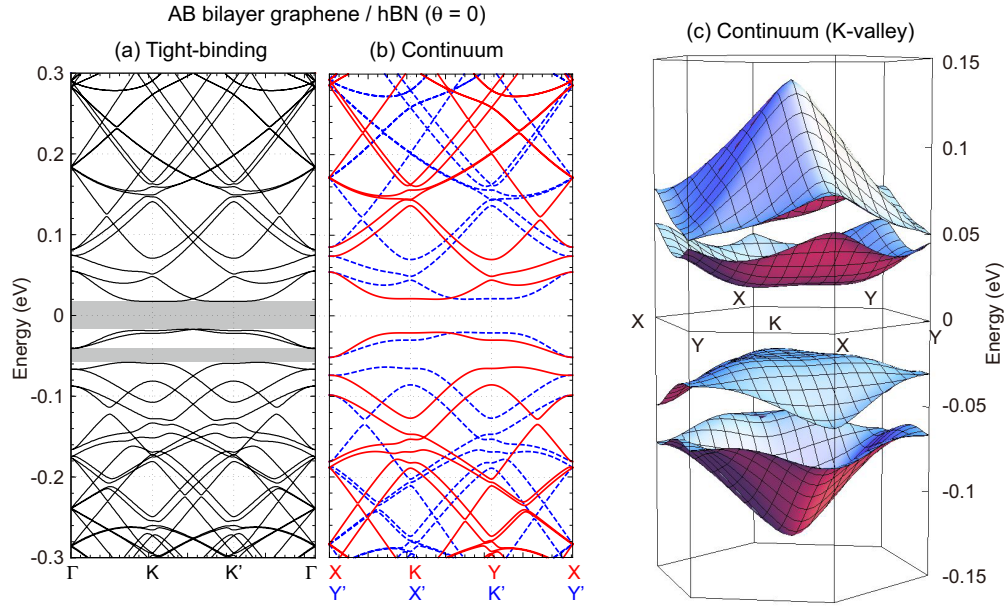
FIG. 5. (Color online) Plots similar to Fig. 3, calculated for AB-bilayer graphene/hBN system with $\theta = 0°$.

gap between the first band and the second band, and it is larger on the hole side than on the electron side similar to the monolayer graphene-hBN system. The recent experiment observed consistent features where a stronger resistance peak appeared on the hole side [24].

IV. SPECTRUM IN MAGNETIC FIELD

We calculate the energy spectrum of monolayer graphene on a hBN system under a uniform perpendicular magnetic field. Here we use the tight-binding lattice Hamiltonian [12] with a Peierls phase

$$\phi_{ij} = -\frac{e}{\hbar} \int_j^i \mathbf{A}(\mathbf{r}) \cdot d\mathbf{r} \qquad (28)$$

between sites i and site j. Here $\mathbf{A}(\mathbf{r}) = (0, Bx, 0)$ is the vector potential giving a uniform magnetic field B perpendicular to the layers. We take the wave functions of low-lying Landau levels of monolayer in $|\varepsilon| \lesssim 1.0$ eV, and compose the Hamiltonian matrix by writing H in terms of the reduced basis [12]. For simplicity, we neglected spin Zeeman splitting throughout the calculation.

Figure 6(a) shows the energy spectrum of graphene monolayer on hBN with $\theta = 0°$, as a function of magnetic field strength, with the magnetic flux per a superlattice unit cell Φ measured in units of $\Phi_0 = h/e$. The quantized Hall conductivity inside the energy gaps are represented by numbers in units of $-e^2/h$ as well as shading filling the gaps. While we concentrate on $\theta = 0°$ in the following discussions, the spectrum should look similar in other twist angles θ ($<10°$) except for the characteristic energy scale, as naturally expected from the similarity in the zero-field band structures in Fig. 4.

On the electron side, the spectrum can be viewed as the Landau levels of intrinsic monolayer graphene with the fine structure inside, while on the hole side, in contrast, the monolayer's Landau levels are completely reconstructed into the fractal spectrum. This feature coincides with the zero-field

band structure, Fig. 3, in which the hole side is strongly modified by a large gap opening at the mini-Dirac point. Figure 6(b) shows the spectrum near zeroth Landau level. The width of the modulated Landau level rapidly grows in the high field region $B > 10$ T, where the minigap structure inside the level becomes significant.

In a pristine monolayer graphene, the Landau levels are completely valley (K, K') degenerate because of the intrinsic inversion symmetry [54]. As a result, the quantized Hall conductivity can only have the values of $4m + 2$ ($m \in \mathbb{Z}$), where the factor 4 is from the spin-valley degeneracy. In monolayer on a hBN system, the valley degeneracy is broken by the inversion asymmetric V_{hBN}. In Fig. 6(d), we plot the energy spectrum with different shadings (colors) for K and K' valleys. We can see that the degeneracy between K and K' levels is actually lifted, and the levels from different valleys simply cross each other, since the two valleys are hardly hybridized by the superlattice potential. As a consequence of the valley splitting, we have the Hall conductivity $4m$ outside the standard sequence of monolayer graphene, as seen in Figs. 6(a) and 6(b).

When the Dirac point in graphene is gapped by a time-reversal symmetric potential, generally, the zeroth Landau level of one valley sticks to the top of the gap, while that of the other valley sticks to the bottom of the gap [55]. Therefore, a larger energy gap in the Dirac spectrum is always accompanied by the larger valley splitting in the magnetic field. In Fig. 6(d), we actually see a large valley splitting of ~20 meV at the hole-side mini-Dirac point (marked by arrows), which exactly corresponds to the energy gap in the zero-field band structure, Fig. 3. Similarly, the valley splitting of the zeroth Landau level in small B corresponds to a tiny energy gap 2 meV at the central Dirac point.

Figure 6(c) is the Wannier diagram [56], which indicates the positions of energy gaps in the space of charge density n and magnetic field B. The thickness of each line is proportional to the width of the corresponding energy gap. In the Wannier
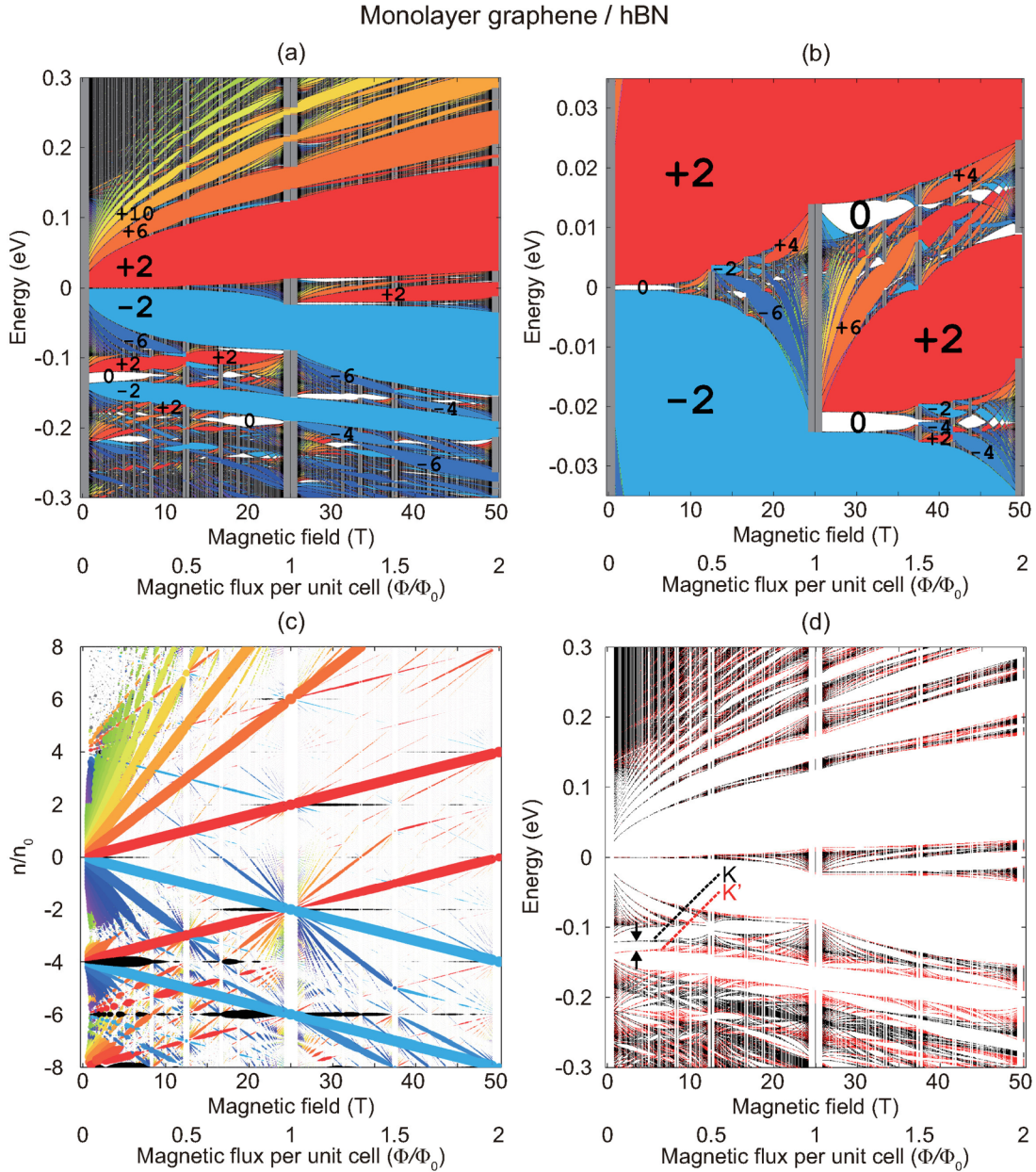
Monolayer graphene / hBN

FIG. 6. (Color online) Energy spectrum of monolayer graphene on a hBN system with $\theta = 0°$ as a function of magnetic field strength in (a) wide and (b) narrow ranges of energy. In each figure, the quantized values of Hall conductivity inside energy gaps are indicated by numbers in units $-e^2/h$ as well as shading filling the gaps. The Hall conductivity of the gray area cannot be determined by the present calculation. (c) Wannier diagram calculated for the energy spectrum in (a). Each gap is plotted as a line of which thickness is proportional to the gap width, and the color represents the quantized Hall conductivity. The color map for the Hall conductivity is the same as that in (a) and (b), except that the black circle represents the gap with Hall conductivity 0 in (c). (d) Energy spectrum originating from monolayer's K region (black) and K' region (red).

diagram, each single energy gap always follows a linear trajectory [57,58]

$$\frac{n}{n_0} = t\frac{\Phi}{\Phi_0} + s, \qquad (29)$$

where n is the electron density, $n_0 = 1/S$ is the electron density per each Bloch band, and t and s are topologically invariant integers. The quantized Hall conductivity is given by $-te^2/h$ [57,58]. In the vicinity of the Dirac point at weak-field regime, we see a conventional Landau fan diagram where the gap

trajectories originate from the charge neutral point at $B = 0$ (i.e., $s = 0$). In a fractal band regime, on the other hand, we see a different series of trajectories having nonzero y intercept (i.e., $s \neq 0$) at $B = 0$, which are an evidence of Hofstadter's spectrum [24]. In accordance with the large gap opening at the mini-Dirac point of the hole side, we have strong signals from the mini-Landau fan centered at $n/n_0 = -4$. At the cross points with the conventional Landau fan and mini-Landau fan (e.g., $n/n_0 = -2$ at $\Phi/\Phi_0 = 1$) we have the second generation of the Landau fan as a part of the recursive structure.
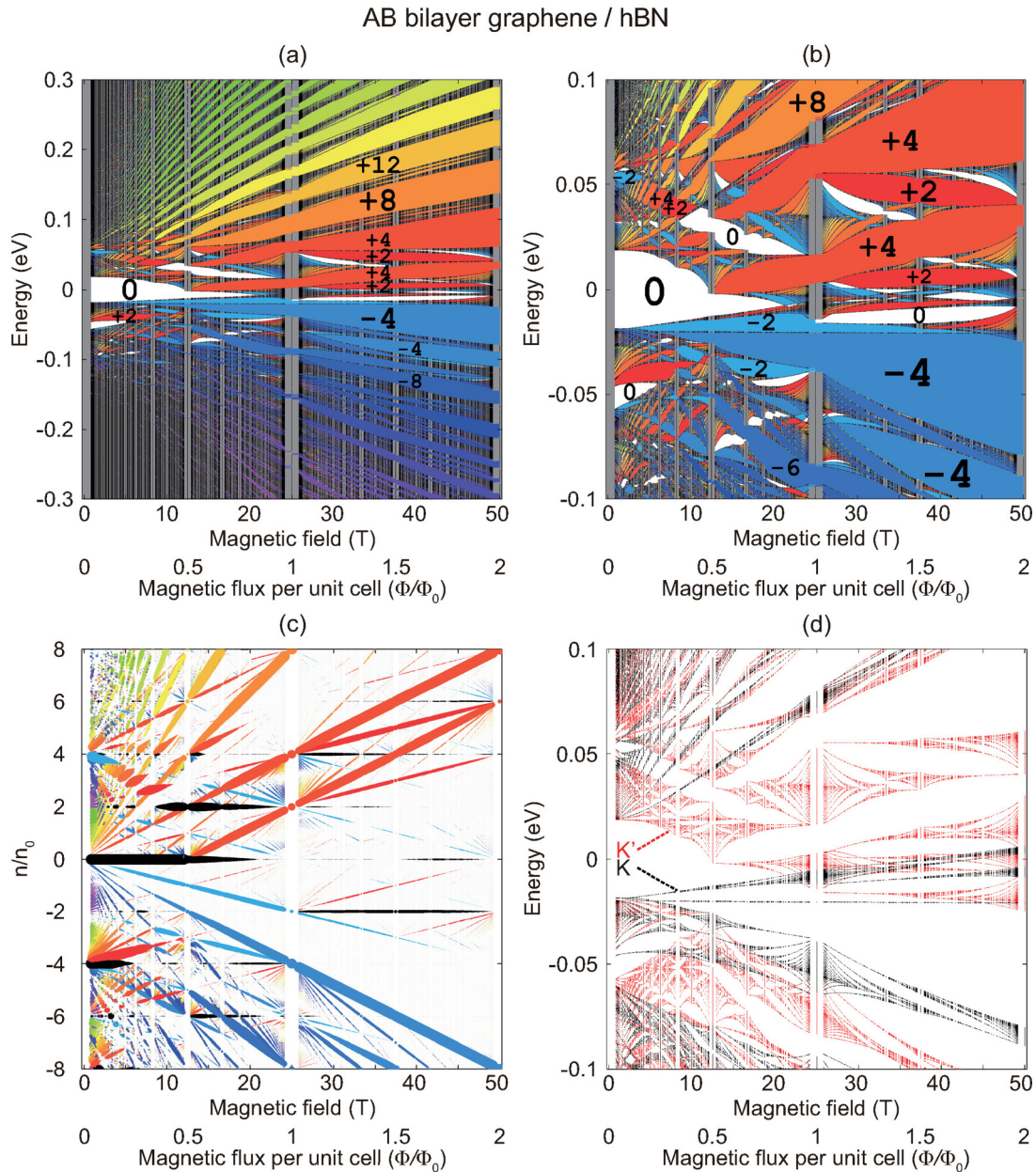
FIG. 7. (Color online) Plots similar to Fig. 6 for AB-stacked bilayer graphene on a hBN system with $\theta = 0°$.

Figures 7(a) and 7(b) show the energy spectrum of AB-stacked bilayer graphene on a hBN system with $\theta = 0°$ and quantized Hall conductivity in the magnetic field. The spectrum in the low-energy region $|E| < 0.1$ eV exhibits a complicated fractal structure, corresponding to the strong modification in the zero-field band structure. In the valley separated spectrum, Fig. 7(d), the valley splitting is much greater than in the monolayer-hBN case. The spectra of K and K' exhibit completely different configurations, and cannot be regarded as a shifted pair of the same spectrum. In a bilayer-hBN system, only a single layer out of two graphene layers feels the effective potential of hBN, and it severely breaks the inversion symmetry which swaps the two layers. In a monolayer-hBN system, in contrast, the inversion symmetry breaking solely comes from **r** dependence of $V_{\text{hBN}}(\mathbf{r})$, and the effect is relatively minor.

The complicated level structure in a bilayer-hBN system can be better understood by comparing the spectrum to Fig. 8, which plots the Landau levels of the bilayer graphene with interlayer asymmetric potential V_0 and 0 for the layer 1 and 2, respectively (the origin of the energy axis is set to the gap center). This corresponds to the situation where we neglect all the spatially-modulating terms in V_{hBN}, leaving only the constant term V_0. The central energy gap and the valley splitting of $n = -1,0$ levels roughly coincide with the properties in the original spectrum. In addition, among the four levels ($n = -1,0$ at K and K') which comprise the lowest Landau levels, only the two levels of K' evolve into a clear fractal spectrum, and the other two of K remain almost intact. This is because the wave function of the zero-energy Landau levels ($n = -1,0$) in bilayer graphene are layer polarized depending on the valley: K levels are localized on layer 2
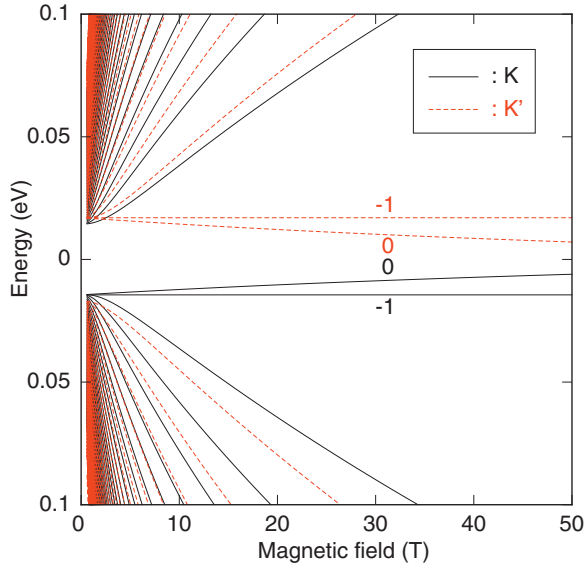
FIG. 8. (Color online) Landau level structure in bilayer graphene with the interlayer potential asymmetry $\pm V_0/2$.

while K' levels are on layer 1. Since the hBN layer influences layer 1, the fractal evolution of the spectrum is much clearer in K' than K. In K valley, we see that the $n = -1$ level remains almost Landau level-like, while the $n = 0$ level exhibits a small minigap structure. This is because the wave function of $n = -1$ is almost completely localized on layer 2, while the state with $n = 0$ has small amplitude on layer 1, which is proportional to interlayer asymmetric potential V_0 [55,59].

The lift of valley degeneracy directly affects the quantized value of the Hall conductivity in Figs. 7(a), 7(b), and 7(c). In regular bilayer graphene, the Hall conductivity can take the values of $4m$ ($m \in \mathbb{Z}$), where the factor 4 is from the spin-valley degeneracy. In moiré system $4m + 2$ can also appear due to the valley splitting [24].

It should be noted that the Hofstadter butterfly in this work arises from the competition between the long-period moiré superlattice potential (of the order of 1–100 nm) and magnetic field. On the other hand, there is another rich spectral structure which comes from the competition between the atomic lattice period of constituent layers (order of 0.1 nm) and magnetic field [60,61]. Considering the condition for the
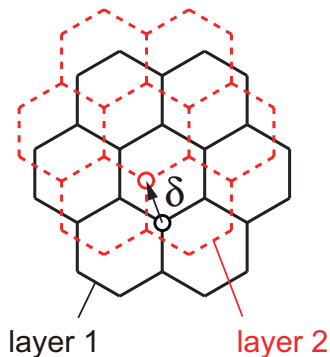

FIG. 9. (Color online) Nonrotated, shifted bilayer of tight-binding honeycomb lattices with the same lattice constant.

fractal spectrum, $Ba^2/(h/e) \sim 1$, the latter effect becomes conspicuous in a relatively high magnetic field range. In the present calculation, both interference effects are fully taken into account in the tight-binding Hamiltonian, while the effect of the atomic periodicity is almost negligible in the magnetic range of 0–50 T considered here.

V. CONCLUSION

We calculated the band structures of moiré systems composed of monolayer and bilayer graphene on the hBN layer. We developed an effective continuum theory in the framework of a tight-binding method and analytically investigated several characteristic properties in the band structure. We showed that the inversion-asymmetric term generally opens an energy gap both at the intrinsic Dirac point and the mini-Dirac point, and the gap width exhibits a strong electron-hole asymmetry. We investigated the energy spectrum and quantum Hall effect of graphene-hBN systems in uniform magnetic field, and demonstrated the evolution of the fractal spectrum as a function of the magnetic field. The lack of the inversion symmetry is responsible for the breaking of the valley degree of freedom. The valley splitting is more significant in bilayer graphene on hBN than in monolayer graphene on hBN because of the stronger inversion-symmetry breaking in a bilayer-hBN system.

APPENDIX A: INTERLAYER COUPLING IN NONROTATED BILAYER OF HONEYCOMB LATTICES

Here we derive the interlayer coupling Hamiltonian for a nonrotated, shifted bilayer of tight-binding honeycomb lattices. We assume the two layers are identical honeycomb lattices with the same lattice constant, and they are arranged in parallel fashion with a constant in-plane displacement $\boldsymbol{\delta}$ and interlayer spacing d, as illustrated in Fig. 9. The unit cell includes A_l and B_l for the layer $l = 1,2$. We assume that the transfer integral between any two sites is given by Eq. (9).

We define the Bloch wave basis of a single layer as

$$|\mathbf{k}, X_l\rangle = \frac{1}{\sqrt{N}} \sum_{\mathbf{R}_{X_l}} e^{i\mathbf{k}\cdot\mathbf{R}_{X_l}} |\mathbf{R}_{X_l}\rangle, \tag{A1}$$

where $\mathbf{k}$ is the Bloch wave vector, $X = A, B$ is the sublattice index, $l = 1,2$ is the layer index, and N is the number of monolayer graphene unit cells (containing a single pair of A and B sites) in the whole system. The interlayer matrix element is then written as

$$\begin{aligned}
U_{A_2 A_1}(\mathbf{k}, \boldsymbol{\delta}) &\equiv \langle \mathbf{k}, A_2 | H | \mathbf{k}, A_1 \rangle = u(\mathbf{k}, \boldsymbol{\delta}), \\
U_{B_2 B_1}(\mathbf{k}, \boldsymbol{\delta}) &\equiv \langle \mathbf{k}, B_2 | H | \mathbf{k}, B_1 \rangle = u(\mathbf{k}, \boldsymbol{\delta}), \\
U_{B_2 A_1}(\mathbf{k}, \boldsymbol{\delta}) &\equiv \langle \mathbf{k}, B_2 | H | \mathbf{k}, A_1 \rangle = u(\mathbf{k}, \boldsymbol{\delta} - \boldsymbol{\tau}_1), \\
U_{A_2 B_1}(\mathbf{k}, \boldsymbol{\delta}) &\equiv \langle \mathbf{k}, A_2 | H | \mathbf{k}, B_1 \rangle = u(\mathbf{k}, \boldsymbol{\delta} + \boldsymbol{\tau}_1),
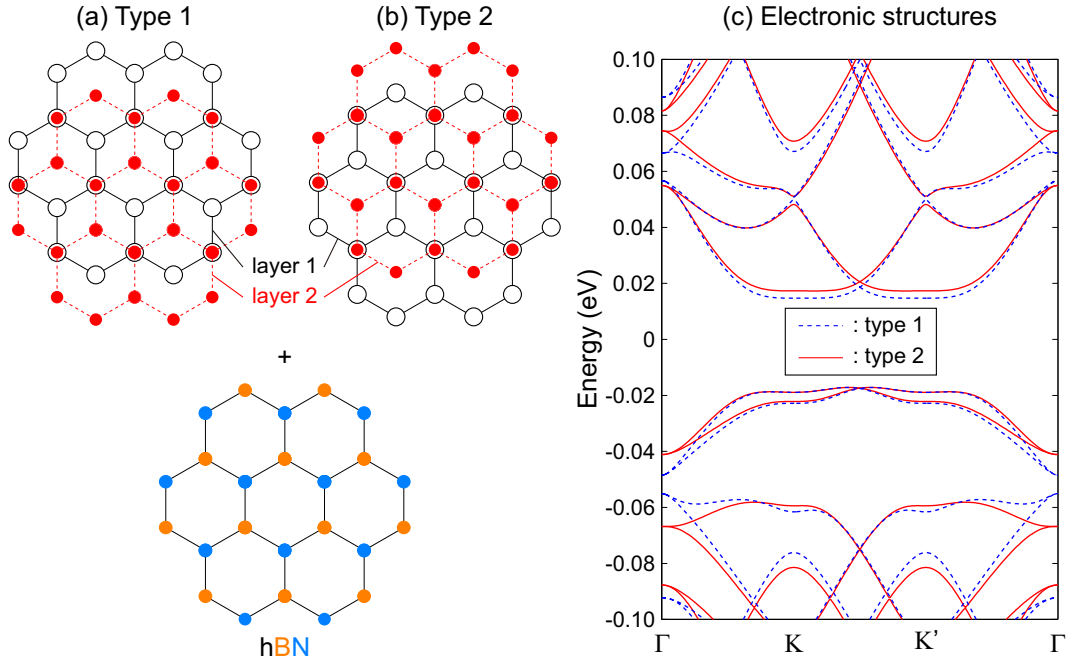\end{aligned} \tag{A2}$$

FIG. 10. (Color online) (a) and (b): two different configurations of AB-stacked bilayer graphene on a hBN layer. (c) Electronic structures of the configurations (a) (dotted blue) and (b) (solid red).

where

$$u(\mathbf{k},\boldsymbol{\delta}) = \sum_{n_1,n_2} -t(n_1\mathbf{a}_1 + n_2\mathbf{a}_2 + \mathbf{d}_z + \boldsymbol{\delta})$$
$$\times \exp[-i\mathbf{k}\cdot(n_1\mathbf{a}_1 + n_2\mathbf{a}_2 + \boldsymbol{\delta})], \quad \text{(A3)}$$

and $\boldsymbol{\tau}_1 = (-\mathbf{a}_1 + 2\mathbf{a}_2)/3$ is a vector connecting the nearest A and B sublattices, and $\mathbf{d}_z = d_{\text{G-hBN}}\,\mathbf{e}_z$ is the perpendicular displacement between graphene and hBN.

The function $u(\mathbf{k},\boldsymbol{\delta})$ is obviously periodic in $\boldsymbol{\delta}$ with periods $\mathbf{a}_1$ and $\mathbf{a}_2$, and it is then Fourier transformed as

$$u(\mathbf{k},\boldsymbol{\delta}) = \sum_{m_1,m_2} \tilde{t}(m_1\mathbf{a}_1^* + m_2\mathbf{a}_2^* + \mathbf{k})$$
$$\times \exp[i(m_1\mathbf{a}_1^* + m_2\mathbf{a}_2^*)\cdot\boldsymbol{\delta}], \quad \text{(A4)}$$

where $\tilde{t}(\mathbf{q})$ is the in-plane Fourier transform of $t(\mathbf{R})$ defined by

$$\tilde{t}(\mathbf{q}) = \frac{1}{S}\int t(\mathbf{R} + \mathbf{d}_z)e^{-i\mathbf{q}\cdot\mathbf{R}}d\mathbf{R}, \quad \text{(A5)}$$

with $S = |\mathbf{a}_1 \times \mathbf{a}_2|$, and the integral in $\mathbf{R}$ is taken over an infinite two-dimensional space. In the present tight-binding model, $t(\mathbf{R})$ exponentially decays in $R \gtrsim r_0$, so that the Fourier transform $\tilde{t}(\mathbf{q})$ decays in $q \gtrsim 1/r_0$. In Eq. (A4), therefore, we only need to take a few Fourier components within $|m_1\mathbf{a}_1^* + m_2\mathbf{a}_2^* + \mathbf{k}| \lesssim O(1/r_0)$.

In the following we only consider the electronic states near $\mathbf{K}_\xi$ point, and then we can approximate $u(\mathbf{k},\boldsymbol{\delta})$ with $u(\mathbf{K}_\xi,\boldsymbol{\delta})$. Equation (A4) then becomes

$$u(\mathbf{K}_\xi,\boldsymbol{\delta}) \approx u_0[1 + e^{i\xi\mathbf{a}_1^*\cdot\boldsymbol{\delta}} + e^{i\xi(\mathbf{a}_1^*+\mathbf{a}_2^*)\cdot\boldsymbol{\delta}}], \quad \text{(A6)}$$

with

$$u_0 = \tilde{t}(\mathbf{K}_\xi), \quad \text{(A7)}$$

which gives Eq. (14). In the present tight-binding parameter, we have $u_0 \approx 0.152$ eV. The second largest Fourier component is $\tilde{t}(2\mathbf{K}_\xi) \approx 0.0025$ eV and is safely neglected.

Finally, Eq. (A2) becomes

$$U_{A_2A_1} = U_{B_2B_1} = u_0[1 + e^{i\xi\mathbf{a}_1^*\cdot\boldsymbol{\delta}} + e^{i\xi(\mathbf{a}_1^*+\mathbf{a}_2^*)\cdot\boldsymbol{\delta}}],$$
$$U_{B_2A_1} = u_0[1 + \omega^\xi e^{i\xi\mathbf{a}_1^*\cdot\boldsymbol{\delta}} + \omega^{-\xi} e^{i\xi(\mathbf{a}_1^*+\mathbf{a}_2^*)\cdot\boldsymbol{\delta}}], \quad \text{(A8)}$$
$$U_{A_2B_1} = u_0[1 + \omega^{-\xi} e^{i\xi\mathbf{a}_1^*\cdot\boldsymbol{\delta}} + \omega^\xi e^{i\xi(\mathbf{a}_1^*+\mathbf{a}_2^*)\cdot\boldsymbol{\delta}}].$$

In the moire system, $\boldsymbol{\delta}$ is not constant but slowly depends on the position $\mathbf{r}$. By replacing $\boldsymbol{\delta}$ in Eq. (A8) with $\boldsymbol{\delta}(\mathbf{r})$ in Eq. (2), we obtain the interlayer Hamiltonian U for the moiré system, Eq. (13). Here we used the relation $\mathbf{a}_i^* \cdot \boldsymbol{\delta} = \mathbf{G}_i^M \cdot \mathbf{r}$.

APPENDIX B: AB BILAYER AND BA BILAYER WITH HBN

For AB-stacked bilayer + hBN system, we have two different stacking geometries illustrated by Figs. 10(a) and 10(b), which we call type 1 and type 2, respectively. The effective Hamiltonian for type 1 is given by Eq. (25), and for type 2 is

$$\mathcal{H}_{\text{BLG-hBN}}^{\text{(type2)}} = \begin{pmatrix} H_{\text{G}} + V_{\text{hBN}} & U_{\text{BLG}} \\ U_{\text{BLG}}^\dagger & H_{\text{G}} \end{pmatrix}, \quad \text{(B1)}$$

which is actually distinct from Eq. (25) in that the off-diagonal blocks are interchanged. Figure 10(c) compares the energy spectra of type 1 and type 2, calculated by the tight-binding model and the effective continuum model. There are small but finite differences in the band structures, especially at the BZ boundary.

[1] C. Berger, Z. Song, X. Li, X. Wu, N. Brown, C. Naud, D. Mayou, T. Li, J. Hass, A. N. Marchenkov, E. H. Conrad, P. N. First, and W. A. de Heer, Science **312**, 1191 (2006).

[2] J. M. B. Lopes dos Santos, N. M. R. Peres, and A. H. Castro Neto, Phys. Rev. Lett. **99**, 256802 (2007).

[3] G. Trambly de Laissardière, D. Mayou, and L. Magaud, Nano Lett. **10**, 804 (2010).

[4] S. Shallcross, S. Sharma, E. Kandelaki, and O. A. Pankratov, Phys. Rev. B **81**, 165105 (2010).

[5] E. S. Morell, J. D. Correa, P. Vargas, M. Pacheco, and Z. Barticevic, Phys. Rev. B **82**, 121407(R) (2010).

[6] R. Bistritzer and A. MacDonald, Proc. Natl. Acad. Sci. **108**, 12233 (2011).

[7] M. Kindermann and P. N. First, Phys. Rev. B **83**, 045425 (2011).

[8] L. Xian, S. Barraza-Lopez, and M. Y. Chou, Phys. Rev. B **84**, 075425 (2011).

[9] J. M. B. Lopes dos Santos, N. M. R. Peres, and A. H. Castro Neto, Phys. Rev. B **86**, 155449 (2012).

[10] P. Moon and M. Koshino, Phys. Rev. B **87**, 205404 (2013).

[11] D. Hofstadter, Phys. Rev. B **14**, 2239 (1976).

[12] P. Moon and M. Koshino, Phys. Rev. B **85**, 195458 (2012).

[13] P. Moon and M. Koshino, Phys. Rev. B **88**, 241412 (2013).

[14] R. Bistritzer and A. H. MacDonald, Phys. Rev. B **84**, 035440 (2011).

[15] C. R. Dean, A. F. Young, I. Meric, C. Lee, L. Wang, S. Sorgenfrei, K. Watanabe, T. Taniguchi, P. Kim, K. L. Shepard, and J. Hone, Nat. Nanotechnol. **5**, 722 (2010).

[16] J. Xue, J. Sanchez-Yamagishi, D. Bulmash, P. Jacquod, A. Deshpande, K. Watanabe, T. Taniguchi, P. Jarillo-Herrero, and B. LeRoy, Nat. Mater. **10**, 282 (2011).

[17] M. Yankowitz, J. Xue, D. Cormode, J. D. Sanchez-Yamagishi, K. Watanabe, T. Taniguchi, P. Jarillo-Herrero, P. Jacquod, and B. J. LeRoy, Nat. Phys. **8**, 382 (2012).

[18] L. Ponomarenko, R. Gorbachev, G. Yu, D. Elias, R. Jalil, A. Patel, A. Mishchenko, A. Mayorov, C. Woods, J. Wallbank *et al.*, Nature (London) **497**, 594 (2013).

[19] B. Hunt, J. D. Sanchez-Yamagishi, A. F. Young, M. Yankowitz, B. J. LeRoy, K. Watanabe, T. Taniguchi, P. Moon, M. Koshino, P. Jarillo-Herrero, and R. C. Ashoori, Science **340**, 1427 (2013).

[20] G. L. Yu, R. V. Gorbachev, J. S. Tu, A. V. Kretinin, Y. Cao, R. Jalil, F. Withers, L. A. Ponomarenko, B. A. Piot, M. Potemski, D. C. Elias, X. Chen, K. Watanabe, T. Taniguchi, I. V. Grigorieva, K. S. Novoselov, V. I. Fal'ko, A. K. Geim, and A. Mishchenko, Nat. Physics **10**, 525 (2014).

[21] M. Yankowitz, J. Xue, and B. J. LeRoy, J. Phys.: Condens. Matter **26**, 303201 (2014).

[22] K. Watanabe, T. Taniguchi, and H. Kanda, Nat. Mater. **3**, 404 (2004).

[23] Y. Kubota, K. Watanabe, O. Tsuda, and T. Taniguchi, Science **317**, 932 (2007).

[24] C. R. Dean, L. Wang, P. Maher, C. Forsythe, F. Ghahari, Y. Gao, J. Katoch, M. Ishigami, P. Moon, M. Koshino, T. Taniguchi, K. Watanabe, K. L. Shepard, J. Hone, and P. Kim, Nature (London) **497**, 598 (2013).

[25] B. Sachs, T. O. Wehling, M. I Katsnelson, and A. I. Lichtenstein, Phys. Rev. B **84**, 195414 (2011).

[26] M. Kindermann, B. Uchoa, and D. L. Miller, Phys. Rev. B **86**, 115415 (2012).

[27] C. Ortix, L. Yang, and J. van den Brink, Phys. Rev. B **86**, 081405 (2012).

[28] J. R. Wallbank, A. A. Patel, M. Mucha-Kruczyński, A. K. Geim, and V. I. Fal'ko, Phys. Rev. B **87**, 245408 (2013).

[29] M. Mucha-Kruczyński, J. R. Wallbank, and V. I. Fal'ko, Phys. Rev. B **88**, 205418 (2013).

[30] X. Chen, J. R. Wallbank, A. A. Patel, M. Mucha-Kruczyński, E. McCann, and V. I. Fal'ko, Phys. Rev. B **89**, 075401 (2014).

[31] M. Bokdam, T. Amlaki, G. Brocks, and P. J. Kelly, Phys. Rev. B **89**, 201404 (2014).

[32] J. Jung, A. Raoux, Z. Qiao, and A. H. MacDonald, arXiv:1312.7723.

[33] P. San-Jose, A. Gutiérrez-Rubio, M. Sturla, and F. Guinea, Phys. Rev. B **90**, 075428 (2014).

[34] J. C. Song, P. Samutpraphoot, and L. S. Levitov, arXiv:1404.4019.

[35] B. Uchoa, V. N. Kotov, and M. Kindermann, arXiv:1404.5005.

[36] M. Neek-Amal and F. Peeters, Appl. Phys. Lett. **104**, 041909 (2014).

[37] L. Brey, Phys. Rev. Applied **2**, 014003 (2014).

[38] L. Liu, Y. P. Feng, and Z. X. Shen, Phys. Rev. B **68**, 104102 (2003).

[39] G. Giovannetti, P. A. Khomyakov, G. Brocks, P. J. Kelly, and J. van den Brink, Phys. Rev. B **76**, 073103 (2007).

[40] J. Sławińska, I. Zasada, and Z. Klusek, Phys. Rev. B **81**, 155433 (2010).

[41] T. Nakanishi and T. Ando, J. Phys. Soc. Jpn. **70**, 1647 (2001).

[42] S. Uryu, Phys. Rev. B **69**, 075402 (2004).

[43] J. Slater and G. Koster, Phys. Rev. **94**, 1498 (1954).

[44] J. McClure, Phys. Rev. **104**, 666 (1956).

[45] D. P. DiVincenzo and E. J. Mele, Phys. Rev. B **29**, 1685 (1984).

[46] G. W. Semenoff, Phys. Rev. Lett. **53**, 2449 (1984).

[47] N. H. Shon and T. Ando, J. Phys. Soc. Jpn. **67**, 2421 (1998).

[48] T. Ando, J. Phys. Soc. Jpn. **74**, 777 (2005).

[49] E. McCann and V. I. Fal'ko, Phys. Rev. Lett. **96**, 086805 (2006).

[50] C. R. Woods, L. Britnell, A. Eckmann, R. S. Ma, J. C. Lu, H. M. Guo, X. Lin, G. L. Yu, Y. Cao, R. V. Gorbachev, A. V. Kretinin, J. Park, L. A. Ponomarenko, M. I. Katsnelson, Yu. N. Gornostyrev, K. Watanabe, T. Taniguchi, C. Casiraghi, H.-J. Gao, A. K. Geim, and K. S. Novoselov, Nat. Phys. **10**, 451 (2014).

[51] F. D. M. Haldane, Phys. Rev. Lett. **93**, 206602 (2004).

[52] L. Fu and C. L. Kane, Phys. Rev. B **76**, 045302 (2007).

[53] M. Koshino, Phys. Rev. B **88**, 115409 (2013).

[54] M. Koshino and E. McCann, Phys. Rev. B **81**, 115315 (2010).

[55] M. Koshino and T. Ando, Phys. Rev. B **81**, 195431 (2010).

[56] G. Wannier, Phys. Status Solidi (b) **88**, 757 (1978).

[57] M. Kohmoto, Ann. Phys. **160**, 343 (1985).

[58] D. J. Thouless, M. Kohmoto, M. P. Nightingale, and M. den Nijs, Phys. Rev. Lett. **49**, 405 (1982).

[59] M. Koshino and E. McCann, Phys. Rev. B **83**, 165443 (2011).

[60] Y. Hasegawa and M. Kohmoto, Phys. Rev. B **88**, 125426 (2013).

[61] J. G. Pedersen and T. G. Pedersen, Phys. Rev. B **87**, 235404 (2013).